NJC

PAPER

View Article Online
View Journal | View Issue

Cite this: *New J. Chem.*, 2015, 39, 6531

An insight into local environment of lanthanide ions in Sr_2SiO_4:Ln (Ln = Sm, Eu and Dy)†

Santosh K. Gupta,*[a] Sandeep Nigam,[b] Ashok K. Yadav,[c] Manoj Mohapatra,[a] Shambhu N. Jha,[b] Chiranjib Majumder[b] and Dibyendu Bhattacharyya[c]

Received (in Victoria, Australia) 11th May 2015,
Accepted 11th June 2015

DOI: 10.1039/c5nj01191d

www.rsc.org/njc

Sr_2SiO_4 is an important inorganic host for lanthanide-doped white-light-emitting diodes. In order to probe the local structure and symmetry around lanthanide ions in Sr_2SiO_4, detailed experimental and theoretical investigations have been carried out. Samples prepared *via* sol–gel methods were thoroughly characterized using X-ray diffraction (XRD), extended X-ray absorption fine structure (EXAFS) and photoluminescence (PL) spectroscopy. The local symmetries of SrO_9 and SrO_{10} polyhedra were determined using emission spectroscopy with europium as the probe ion. Despite having the same oxidation state and comparable ionic radii, Sm^{3+}, Dy^{3+} and Eu^{3+} behave differently in terms of their site occupation at the Sr sites of SrO_9 and SrO_{10} polyhedra. While Eu replaces Sr in both polyhedra, Sm and Dy reside specifically at the 9-coordinated Sr sites only. Based on density functional theory (DFT) calculations, it has been established that for Dy and Sm, the strong metal–oxygen bonding leads to significant distortion and hence the destabilization of MO_{10} polyhedra in the host.

1. Introduction

Strontium silicate is an important luminescence host and has been extensively investigated for white LEDs applications. Park *et al.* synthesized Eu^{2+}-doped Sr_2SiO_4 yellow phosphor, which was found to produce white emission in combination with a blue-emitting GaN single crystal,[1] and its efficiency was found to be better than that of commercially viable white phosphor. It was also reported that co-doping Ce^{3+} in Eu^{2+}-doped Sr_2SiO_4 phosphor also leads to white emission.[2]

A large number of reports have been published recently in the literature relating to the various technological applications of lanthanide ions-doped Sr_2SiO_4 such as in solid-state lighting,[3,4] as a thermochromic material,[5] as a dosimeter,[6] in long-afterglow phosphors,[7] in IR detection[8] and in long-lasting phosphorescence.[9]

Catti *et al.*[10] discussed the crystal structure of Sr_2SiO_4 and reported that its unit cell consists of two different types of strontium ion; nine-coordinated Sr^{2+} (Sr2) and 10-coordinated Sr^{2+} (Sr1). They also discussed the local symmetry of SrO_9 and SrO_{10} and confirmed that SrO_9 is relatively less symmetrical than SrO_{10}, which has a hexagonal symmetry. In systems where multiple doping sites are available (Sr2 and Sr1), spectroscopic information related to local sites and their point symmetry is crucial for optimizing their optical performance for technological applications. Information about site occupancy can only be obtained *via* X-ray diffraction (XRD) at very high dopant ion concentrations ($\geq$5.0%), which may affect the efficiency of the luminescent material by concentration quenching. Therefore, the actual site symmetry of a dopant in a cationic site cannot be revealed from crystallographic data. Especially when these types of inorganic hosts are used to incorporate lanthanide ions for luminescence applications, it becomes extremely important to acquire the knowledge of the site occupancy of a particular Ln^{3+} ion. Further incorporation of Ln^{3+} ions at a particular site leads to changes in the local surrounding environment in the doped host. Understanding these changes in the local environment is quite important for visualizing the overall changes in the host lattice. Furthermore, since luminescence properties are strongly dependent on the local structure around the phosphor, it is of utmost importance to know the local symmetry around the lanthanide ions.

In an individual work, we extensively studied the luminescence properties of Sm^{3+}, Eu^{2+}, Eu^{3+} and Dy^{3+}.[11–14] Studying the local site occupancy of lanthanide or any dopant ion in a system wherein multiple coordinations or sites are available is very important for correlation between structural and various properties, *viz.* optical, magnetic, and catalytic. These properties are strongly influenced by local structure and site symmetry.

In the present study, we have given a complete picture of the behavior of lanthanide ions in terms of their site occupancy in Sr_2SiO_4. We carried out an exhaustive experimental and theoretical

[a] *Radiochemistry Division, Bhabha Atomic Research Centre, Mumbai 400085, India. E-mail: santufrnd@gmail.com; Fax: +91-22-25505151; Tel: +91-22-25590636*
[b] *Chemistry Division, Bhabha Atomic Research Centre, Mumbai 400085, India*
[c] *Atomic and molecular physics Division, Bhabha Atomic Research Centre, Mumbai 400085, India*

† Electronic supplementary information (ESI) available. See DOI: 10.1039/c5nj01191d

investigation to obtain in-depth knowledge about the local symmetry of SrO_9 and SrO_{10} polyhedra in Sr_2SiO_4. Furthermore, we aimed to understand the factors responsible for the substitution of Sr ions at different sites by three different rare-earth ions, namely, Sm^{3+}, Dy^{3+} and Eu^{3+}. The choice of these three ions is guided by the fact that a combination of these three ions has the potential to generate white light. Time-resolved fluorescence spectroscopy (TRFS) by using emission spectroscopy, emission kinetics and extended X-ray absorption fine structure (EXAFS) measurements have been used to determine the local environment around three lanthanide ions in an Sr_2SiO_4 host. These experimental results were further substantiated using density functional theory (DFT) calculations.

2. Experimental

2.1. Sample preparation

All the chemicals employed for the sample preparation were of analytical reagent (AR) grade and procured from Sigma Aldrich. Sr_2SiO_4 samples were prepared *via* a sol–gel route using tetraethyl orthosilicate (TEOS) as a Si precursor and strontium nitrate as a Sr precursor. High-purity oxides of Sm, Eu and Dy (SPEX Industries, INC., USA) were used for lanthanide ion doping. Details of the synthesis procedure are mentioned in our earlier study.[11–14] For a Eu^{2+}-doped sample, a Eu^{3+}-doped Sr_2SiO_4 sample was subjected to heating at 600 °C for 6 h under a reducing atmosphere (92% Ar + 8% H_2) for the conversion of Eu^{3+} to Eu^{2+}.

2.2. Instrumentation

The phase purity of the prepared phosphor was confirmed by X-ray diffraction (XRD). Measurements were carried out on a STOE X-ray diffractometer equipped with a scintillation counter and graphite monochromator. Diffraction patterns were obtained using monochromatic Cu K_α radiation (λ = 1.5406 Å) keeping the scan rate at 1 s per step in the scattering angle range (2θ) from 10° to 70°. $K_{\alpha 2}$ reflections were removed by a stripping procedure to obtain accurate lattice constants.

All the luminescence spectra were obtained using an Edinburgh FL920 instrument with a variable frequency of 10–100 Hz equipped with a 150 W xenon lamp and an M300 monochromator. Our systems were equipped with double monochromators in either or both excitation and emission arms. The use of double monochromators increases the linear dispersion, and the stray light suppression is improved compared to that achieved by single monochromators. The system also consists of CD920 integrated control electronics and an S900 detector. Powder samples were dispersed in methanol for measurements. Data acquisition and analysis were carried out by F-900 software provided by Edinburgh Analytical Instruments, UK. A Xenon flash lamp with a frequency range of 10–100 Hz was used as the excitation source. The emission spectrum for a particular sample was obtained with a lamp frequency of 100 Hz. Multiple scans (at least five) were taken to minimize fluctuations in peak intensity and maximize the S/N ratio. Fluorescence lifetime measurements were based on the well-established time-correlated single-photon counting (TCSPC) technique. EXAFS experiments were performed at the Raja Ramanna Centre for Advanced Technology (RRCAT), Indore, India, at the dispersive beamline BL-8 in transmission mode using the 2.5 GeV 100 mA INDUS-2 synchrotron source. Other related information on instrumentation and sample preparation for EXAFS measurements is mentioned in our earlier reports.[15–17]

3. Results and discussion

3.1. Powder X-ray diffraction (PXRD): phase purity and crystal structure

The purity and crystallinity of the as-prepared Sr_2SiO_4 and Sr_2SiO_4:Ln^{3+} (Ln = Eu, Dy, Sm) samples were characterized using powder X-ray diffraction (XRD). It can be seen from the XRD patterns in Fig. 1 that the diffraction peaks of both Sr_2SiO_4 and Sr_2SiO_4:Ln^{3+} (Ln = Eu, Dy, Sm) samples could be indexed to the orthorhombic phase of α′-Sr_2SiO_4 (JCPDS card No. 39-1256).

XRD data consisting of *hkl* values and an interplanar spacing corresponding to α′-Sr_2SiO_4 were also evaluated (ESI,† Table T1). The incorporation of lanthanide ions does not change the XRD pattern, which confirms that doping is appropriate and has not distorted the structure of strontium silicate. As no impurity peaks were observed, it is possible to suggest that both samples are a single phase of α′-Sr_2SiO_4. No obvious shifting of peaks or other impurity phases can be detected in Ln^{3+}-doped samples, which indicates that Ln^{3+} ions are efficiently dissolved in the Sr_2SiO_4 host lattice by replacing Sr^{2+} because of their similar ionic radii and very low levels of doping (0.5 mol%).

Fig. 2 shows the crystal structure of α′-Sr_2SiO_4 and the coordination geometry of the Sr^{2+} ion. Its structure is well described in the literature and shows a close resemblance to the similar non-close-packed K_2SiO_4[18] structure. In one unit cell of α′-Sr_2SiO_4, there are 28 atoms: 8 Sr, 4 Si and 16 O atoms. Out of 8 strontium atoms, 4 are Sr(1) and 4 are Sr(2), *i.e.* the distribution ratio of SrO_9 to SrO_{10} is 50 : 50. Si atoms in SiO_4 tetrahedra form a parallel chain. The Sr(1) sites are arranged in

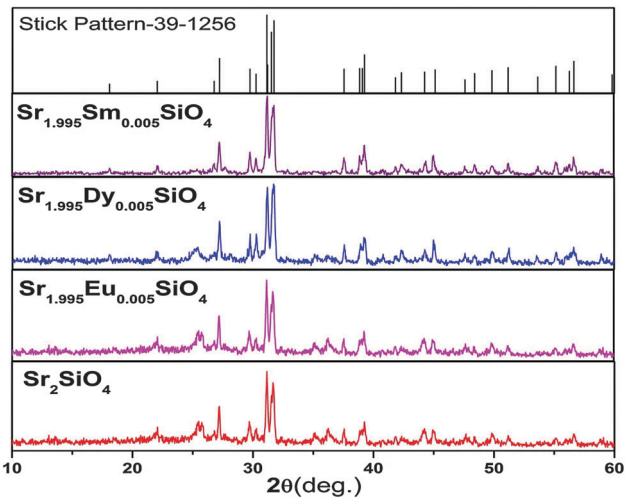

Fig. 1 XRD patterns of Sr_2SiO_4 and Sr_2SiO_4:Ln^{3+} (Ln = Eu, Dy, Sm).

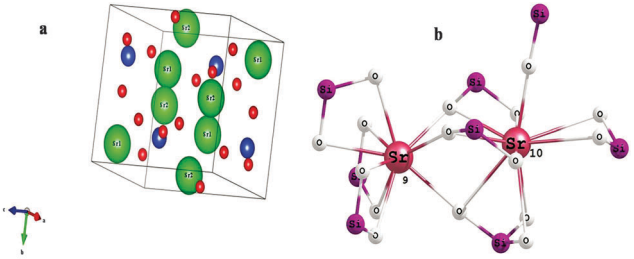

Fig. 2 (a) Crystal structure of α′-Sr_2SiO_4. (b) Schematic of 9- and 10-coordinated Sr^{2+} in strontium silicate.

the form of linear chains (Si–O–Sr(1)–O–Sr(2)), whereas the Sr(2) sites display zigzag patterns of (Sr(1)–O–Sr(2)–O–Sr(1)) along the *b*-axis.[19]

3.2. Photoluminescence investigations

3.2.1. $Sr_2SiO_4:Eu^{3+}$. The excitation spectrum of a 0.5 mol% sample with λ_{em} = 592 nm as presented in Fig. 3 shows an intense and broad band at ~243 nm (41 152 cm^{-1}) and another relatively less intense band at ~296 nm (33 784 cm^{-1}), both of which are assigned to charge transfer bands: CTB-1 and CTB-2, which are respectively due to Sr(2) and Sr(1) polyhedra. In both the cases, the charge transfer is $O^{2-} \rightarrow Eu^{3+}$ only, but oxygens are from different polyhedral, *i.e.* SrO_9 and SrO_{10}. In one case it is Sr_9–O → Eu and in the other case Sr_{10}–O → Eu CT. The peaks that are seen at 320, 360, 380 and 395 nm are due to f–f transitions from the $^7F_0$ ground state to $^5H_3$, $^5L_9$, $^5G_3$ and $^5L_6$ (most intense) levels, respectively. The existence of two charge transfer bands further confirms the presence of two different types of Sr, *i.e.* Sr(1) and Sr(2), in α′-Sr_2SiO_4.

To get an idea of the origin of CTB-1 at 243 nm and CTB-2 at 296 nm, emission spectra were obtained at both the wavelengths and are shown in Fig. 4. The emission spectrum that was acquired at 243 nm shows the typical features of europium ions at 575, 592, 615, 653 and 697 nm due to $^5D_0$ to ^7F_J transitions of Eu^{3+}, where J = 0, 1, 2, 3 and 4, respectively. Among all the transitions that were observed, $^5D_0 \rightarrow {}^7F_1$ at 592 nm and $^5D_0 \rightarrow {}^7F_2$ at 615 nm are special because of their peculiarity as symmetry-sensitive transitions and are generally

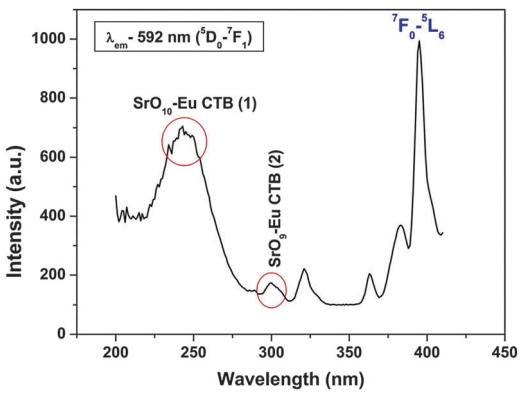

Fig. 3 Excitation spectrum of $Sr_2SiO_4:Eu^{3+}$ (0.5 mol%).

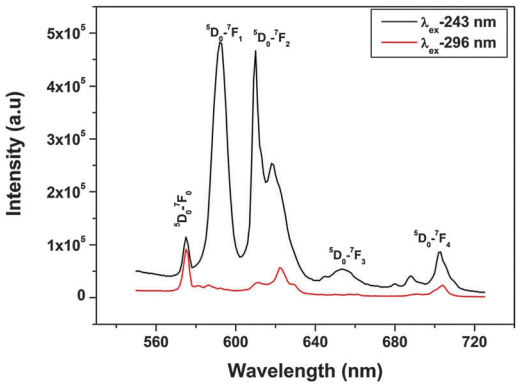

Fig. 4 Emission spectra of $Sr_2SiO_4:Eu^{3+}$ at λ_{ex} = 243 nm and 296 nm.

known as a magnetic dipole transition (MDT) and hypersensitive electric dipole transition (EDT), respectively. In general, at a crystal site with inversion symmetry, EDTs are strictly forbidden and MDT is usually the most intense emission peak; whereas at a site without inversion symmetry, EDT is usually the strongest emission line, because transitions with $\Delta J = \pm 2$ are hypersensitive to small deviations from inversion symmetry. The most sensitive parameter for understanding symmetry is the asymmetry ratio (I), which is defined as the ratio of the integral intensity of EDT ($^5D_0 \rightarrow {}^7F_2$) to that of MDT ($^5D_0 \rightarrow {}^7F_1$). In the spectra obtained at 243 nm excitation, there are two special characteristics: (i) the intensities of $^5D_0 \rightarrow {}^7F_1$ at 592 nm and $^5D_0 \rightarrow {}^7F_2$ at 615 nm are comparable, which is because of the fact that europium ions are distributed at sites with inversion as well as non-inversion symmetry, *i.e.* Sr(1) and Sr(2), and (ii) the presence of a $^5D_0 \rightarrow {}^7F_0$ line, which is forbidden by both electric and magnetic dipole mechanisms, at a higher-energy position (575 nm) than its usual position at around 580 nm. The $^5D_0 \rightarrow {}^7F_0$ transition normally appears when the site symmetry is very low, either C_n or C_{nv}.[20] These two observations confirm that europium occupies both the symmetric Sr(1) site and asymmetric Sr(2) site and excitation at 243 nm excites both the Eu^{3+} ions at Sr(1) and Sr(2) sites.

On the other hand, the emission spectrum that was recorded at 296 nm shows entirely different characteristics. The first and foremost observation is that the intensity of the $^5D_0 \rightarrow {}^7F_0$ transition is higher than that of all the others and the second is the absence of a $^5D_0 \rightarrow {}^7F_1$ magnetic dipole transition. This shows that radiation at 296 nm excites europium ions mostly at relatively asymmetric SrO_9 sites.

It can be inferred from the abovementioned discussion that excitation at 243 and 296 nm, which corresponds to charge transfer (O → Eu) from SrO_{10} and SrO_9, respectively, leads to entirely different emission characteristics. Judging from their respective emission spectra, it appears that radiation at 243 and 296 nm may excite different types of europium ion. To further substantiate the results of emission spectroscopy, photoluminescence decay measurements were carried out. It can be seen from luminescence decay measurements using λ_{ex} of 243 nm (ESI,† Fig. S1) that biexponential behavior with lifetime values of 1.2 ms (fast-decaying, T_1) and 4.7 ms (slow-decaying, T_2) was observed, which indicates the presence of europium ions at two

different sites, whereas monoexponential behavior was observed (ESI,† Fig. S1) on exciting at 296 nm with a lifetime of the order of 1.2 ms (only fast species, T_1). From all these discussions, we can say that there are two types of europium ion: 1.2 ms and 4.7 ms (T_1 and T_2); radiation at 243 nm excites both of them; whereas, radiation at 296 nm selectively excites 1.2 ms (T_1) species only.

Assuming a given phonon energy (the same host for lanthanide ions), a relatively longer PL decay time should be attributed to a more symmetric site, as the f–f transition becomes more forbidden, whereas a shorter decay time is often associated with an asymmetric site due to relaxation in the selection rules. Species T_1 (1.2 ms) arises because of Eu^{3+} ions occupying Sr(2) sites without inversion symmetry, whereas the major species T_1 (4.7 ms) can be ascribed to Eu^{3+} ions occupying Sr(2) sites with inversion symmetry.

To obtain the individual spectra of species T_1 (1.2 ms) and T_2 (4.7 ms), time-resolved emission spectroscopy was carried out using 243 nm as excitation wavelength. Fig. 5 shows the individual TRES spectra of T_1 and T_2, which were derived after appropriate slicing and mathematical calculation (ESI,† Table T2).

It can be seen from the TRES spectra that for long-lived species (T_2), the intensity of MDT is more than that of EDT and the $^5D_0 \rightarrow {}^7F_0$ transition is hardly seen, whereas for short-lived species, $^5D_0 \rightarrow {}^7F_0$ is very intense, large splitting in spectral lines is seen and MDT is absent or negligible. From this observation, we can conclude that T_2 is present at symmetric 10-coordinated Sr(1) sites, whereas T_1 is present at relatively asymmetric 9-coordinated Sr(2) sites.

3.2.2. Symmetry of 9- and 10-coordinated strontium-oxygen polyhedra in α′-Sr_2SiO_4. When Eu^{3+} ions are inserted into any chemical/ligand environment (crystal field), $(2J + 1)$-degenerate J-energy levels split into so-called Stark sub-levels by the ligand field effect and the number of levels depends on the local site symmetry of the metal ion. The substitution of Sr^{2+} by Eu^{3+} may result in significant lattice distortion due to size as well as charge differences. The peak at 575 nm in the lower panel of Fig. 6 is due to $^5D_0 \rightarrow {}^7F_0$ transitions of Eu^{3+} ions. Radiative transitions from $^5D_0$ to levels with $J = 0$ are both ED- and MD-forbidden and only weak transitions from $^5D_0$ to these levels are observed due to the CF-induced J-mixing effect.[20] Moreover, the $^5D_0 \rightarrow {}^7F_0$ transition is only allowed in the following 10 site symmetries: C_s, C_1, C_2, C_3, C_4, C_6, C_{2v}, C_{3v}, C_{4v}, and C_{6v}, according to the ED selection rule.[21]

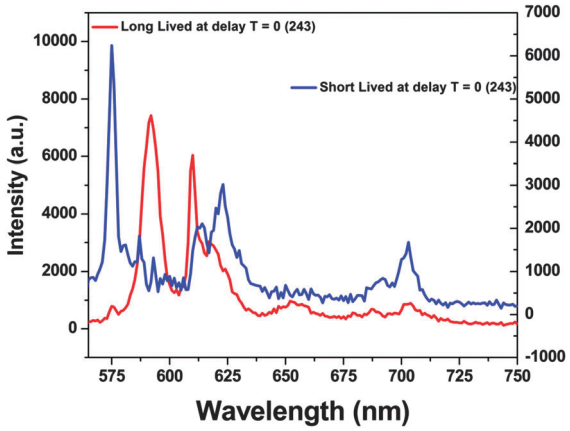

Fig. 5 Emission spectra of the two RE ion species obtained after allowing suitable delay times following TRES measurements (at 243 nm excitation).

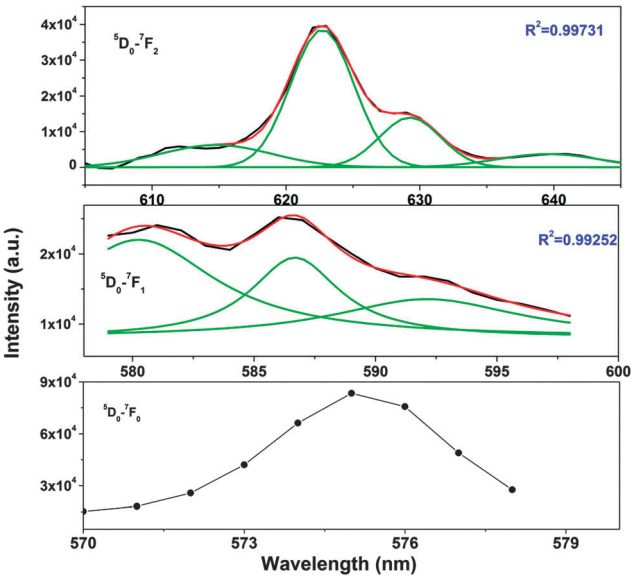

Fig. 6 Gaussian-fitted fluorescence spectra for short-lived Eu^{3+} at 9-coordinated Sr^{2+}. Black lines are experimentally observed, red lines are Gaussian-fitted and green lines indicate deconvoluted components in each case.

From the Stark splitting pattern shown for short-lived species in Fig. 6, one line for the $^5D_0 \rightarrow {}^7F_0$ transition, three lines for the $^5D_0 \rightarrow {}^7F_1$ magnetic dipole transition and four lines for the $^5D_0 \rightarrow {}^7F_0$ electric dipole transition of Eu^{3+} were resolved, whereas for long-lived species as shown in Fig. 7, the $^5D_0 \rightarrow {}^7F_0$ transition is absent but two lines for a $J = 0 \rightarrow J = 1$ transition and three lines for a $J = 0 \rightarrow J = 2$ transition of Eu^{3+} were resolved. According to the branching rules of various point groups,[20–22] it can be inferred that the actual site symmetry of T_1, *i.e.* the actual site symmetry of Eu^{3+} in 9-coordinated Sr–O polyhedra, is C_{2v}, whereas the site symmetry of Eu^{3+} in 10-coordinated Sr–O polyhedra is C_{3v}.

3.2.3. Sr_2SiO_4:Eu^{2+}. Fig. 8a shows the excitation spectrum of Sr_2SiO_4:Eu^{2+} at an emission wavelength of 490 nm. The spectrum displays a broad band at around 340 nm, which is assigned to a $4f^7$ ($^8S_{7/2}$)–$4f^65d^1$ transition of Eu^{2+} ions.

Because Eu^{2+} transitions involve 5d orbitals, an effect due to the crystal field can be seen in their emission spectra. Fig. 8b shows the emission spectrum of Sr_2SiO_4:Eu^{2+} at an excitation wavelength of 340 nm. The spectrum displays two peaks at 490 nm (Eu_1) and 560 nm (Eu_2). This shows the stabilization of Eu^{2+} at two different sites.

The crystal field is related to the ionic radius by the following equation:

$$D_q = \frac{1}{6} Ze^2 \frac{r^4}{R^5} \quad (1)$$

where D_q is the crystal field strength and R is the ionic radius.

It can be seen from the abovementioned equation that the crystal field strength is inversely proportional to the ionic radius.

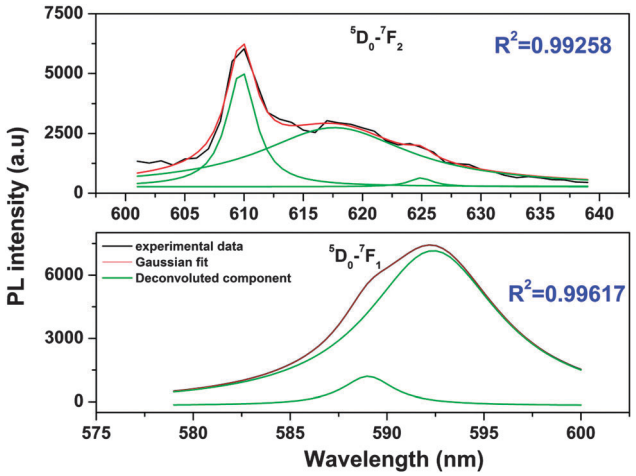

Fig. 7 Gaussian-fitted fluorescence spectra of a selected region for long-lived Eu^{3+} sitting at 10-coordinated Sr^{2+}. Black lines are experimentally observed, red lines are Gaussian-fitted and green lines indicate deconvoluted components in each case.

As in the case of SrO_{10} and SrO_9, the average Sr–O bond lengths are 2.85 and 2.69 Å, respectively, the crystal field strength at Sr9 is higher than at Sr10. Therefore, the crystal field splitting of the d-orbital will be more for Eu at an Sr9 site than at an Sr10 site. As a result, the difference in energy between the lowest electronic levels in the excited state and ground state is greater in the case of Sr10. As a result, more energy is required for the de-excitation of Eu^{2+} at a Sr10 site than at a Sr9 site; therefore, emission occurs at a lower wavelength. The peak at 490 nm is due to $Eu_{Sr(10)}$ and the peak at 550 nm is due to $Eu_{Sr(9)}$.

PL decay corresponding to emissions at 490 and 560 nm (ESI,† Fig. S2), which are due to Eu^{2+} sitting at SrO_{10} sites and SrO_9 sites, respectively, exhibits monoexponential behavior with lifetime values of 0.483 and 1.73 μs.

Based on the phonon energy concept (the same host for lanthanide ions), the longer lifetime should be attributed to the more symmetric site as the electronic transition becomes more forbidden, which corresponds to longer decay times. As discussed in the earlier section, SrO_{10} is more symmetric than SrO_9.

Therefore, the 1.73 μs species arises because Eu^{2+} ions occupy symmetric 10-coordinated Sr(1) sites, whereas the 0.483 μs species is due to Eu^{2+} ions at relatively asymmetric 9-coordinated Sr(2) sites.

3.2.4. Sr_2SiO_4:Dy^{3+}. Fig. 9a shows the photoluminescence excitation spectrum of Sr_2SiO_4:Dy^{3+} for emission at 574 nm. The excitation spectrum consists of sharp lines at 326, 351, 366, 387, 427 and 450 nm, which are attributed to the f–f transitions of the Dy^{3+} ion. The origins of these peaks are labelled in the excitation spectrum itself. The peak at 351 nm is the most intense and is ascribed to $^6H_{15/2} \rightarrow {}^6P_{7/2}$. Fig. 9b shows the emission spectrum of Sr_2SiO_4:Dy^{3+} at 351 nm excitation. The major peaks are located at 480 (blue), 574 (yellow) and 662 nm (red), which are due to $^4F_{9/2} \rightarrow {}^6H_{15/2}$ (blue), $^4F_{9/2} \rightarrow {}^6H_{13/2}$ (yellow) and $^4F_{9/2} \rightarrow {}^6H_{11/2}$ (red) transitions, respectively. The 480 nm peak (blue band) is due to a magnetic dipole transition (MDT) and is generally insensitive to the local site symmetry, whereas the 574 nm peak (yellow band) is a hypersensitive electric dipole transition (ΔJ = 2, EDT) and is strongly affected by the local environment/crystal field around the Dy^{3+} ion. The fact that the 574 nm peak (EDT) is more intense than the 480 nm peak (MDT) indicates that the Dy^{3+} ion is located at a site with low symmetry without any centre of inversion. Based on our discussion, it can be confirmed that in Sr_2SiO_4 on doping, the majority of Dy ions are situated at relatively asymmetric 9-coordinated Sr(2) sites.

Photoluminescence (PL) decay lifetime measurements (ESI,† Fig. S3) of the $^4F_{9/2} \rightarrow {}^6H_{13/2}$ (yellow) transition for the Sr_2SiO_4:Dy^{3+} system at excitation and emission wavelengths of 351 and 574 nm, respectively, show monoexponential behavior. Therefore, in Sr_2SiO_4, Dy^{3+} is homogeneously distributed, occupying relatively asymmetric 9-coordinated Sr sites only.

3.2.5. Sr_2SiO_4:Sm^{3+}. Fig. 10a shows the excitation spectrum of Sr_2SiO_4:Sm^{3+} at an emission wavelength of 605 nm. Fine peaks in the wavelength range of 330–500 nm are displayed, which are due to intra-4f transitions of Sm^{3+} from the $^6H_{5/2}$ ground state to higher energy levels of the samarium ion. There are a number of peaks at 346, 365, 379, 405, 417, 438, 462, 469, 473, and 485 nm, which are ascribed to ($^6H_{5/2} \rightarrow {}^6H_{13/2}$), ($^6H_{5/2} \rightarrow {}^4D_{3/2}$),

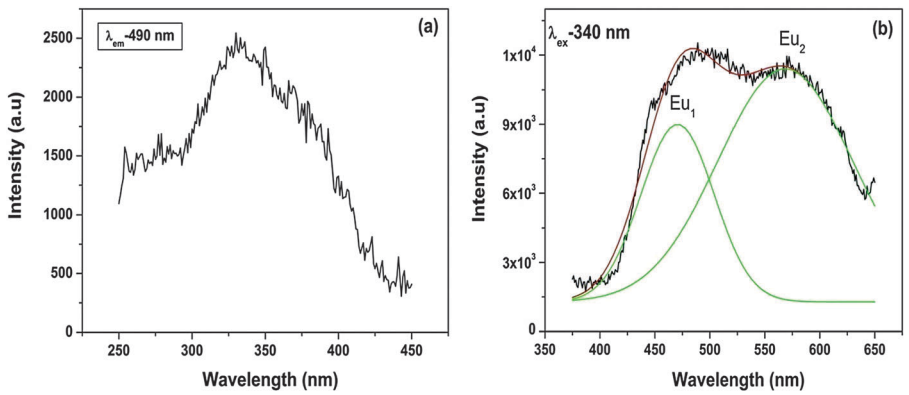

Fig. 8 (a) Excitation spectrum (λ_{em} – 490 nm) and (b) emission spectrum (λ_{ex} – 340 nm) of Sr_2SiO_4:Eu^{2+}. Black lines are experimentally observed, red lines are Gaussian-fitted and green lines indicate deconvoluted components in each case.

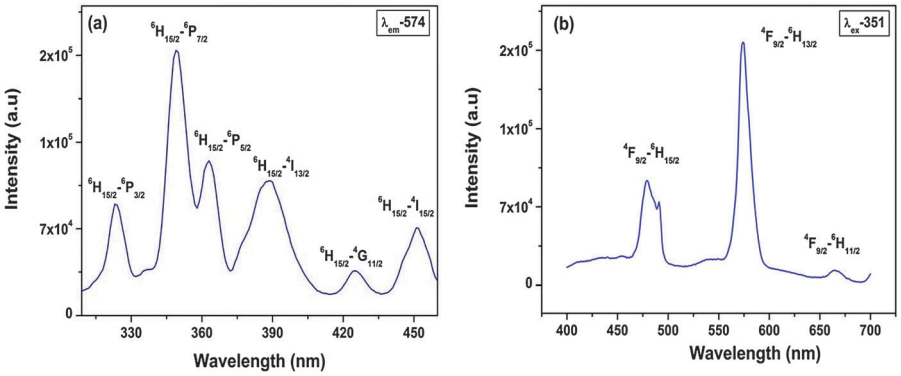

Fig. 9 (a) Excitation and (b) emission spectra of Sr_2SiO_4:Dy^{3+}.

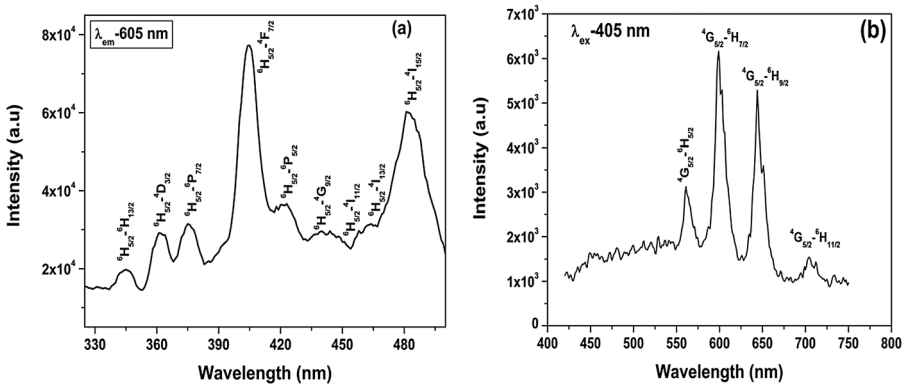

Fig. 10 (a) Excitation and (b) emission spectrum of Sr_2SiO_4:Sm^{3+}.

($^6H_{5/2} \rightarrow {}^6P_{7/2}$), ($^6H_{5/2} \rightarrow {}^4F_{7/2}$), ($^6H_{5/2} \rightarrow {}^6P_{5/2}$), ($^6H_{5/2} \rightarrow {}^4G_{9/2}$), ($^6H_{5/2} \rightarrow {}^4I_{9/2}$), ($^6H_{5/2} \rightarrow {}^4I_{11/2}$), ($^6H_{5/2} \rightarrow {}^4I_{13/2}$) and ($^6H_{5/2} \rightarrow {}^4I_{15/2}$) transitions, respectively. The peak at 405 nm due to the $^6H_{5/2} \rightarrow {}^4F_{7/2}$ transition is the most intense peak. Fig. 10b shows the emission spectrum obtained at 405 nm excitation. This displays the typical emission profile of Sm^{3+}, which consists of peaks at 562, 605, 641 and 711 nm due to $^4G_{5/2} \rightarrow {}^6H_{5/2}$, $^4G_{5/2} \rightarrow {}^6H_{7/2}$, $^4G_{5/2} \rightarrow {}^6H_{9/2}$ and $^4G_{5/2} \rightarrow {}^6H_{11/2}$ transitions, respectively. Among the abovementioned transitions, the one at 562 nm has magnetic dipole character, whereas the one at 641 nm has electric dipole character. The most intense peak at 605 nm is a mixture of magnetic and electric dipole transition. The fact that the electric dipole transition at 641 nm is more intense than the magnetic dipole transition at 562 nm confirms that the majority of Sm^{3+} is stabilized in an asymmetric environment, *i.e.* 9-coordinated Sr(2) sites. The similarity of ionic radii also supports the theory that Sm^{3+} preferentially occupies Sr(2) sites because the difference in size between 9-coordinated Sm^{3+} and 9-coordinated Sr^{2+} is less than that between 10-coordinated Sm^{3+} and Sr^{2+}.

To get a clearer picture of the local site around a Sm^{3+} ion in the strontium silicate host, lifetime measurements at excitation and emission wavelengths of 405 and 605 nm were carried out. The PL decay curve for Sr_2SiO_4:Sm^{3+} (ESI,† Fig. S4) shows a monoexponential profile with a lifetime value of 2.3 ms, which indicates a homogeneous distribution of Sm^{3+} ions in Sr_2SiO_4. Based on fluorescence lifetime and emission spectroscopy results, it can be inferred that Sm^{3+} mainly occupies 9-coordinated Sr(2) sites in Sr_2SiO_4.

3.3. X-ray absorption spectroscopy

3.3.1. Extended X-ray absorption fine structure (EXAFS): normalized and fourier transform. Fig. 11 shows normalized EXAFS spectra ($\mu(E)$ *versus* E) for blank Sr_2SiO_4 along with Eu, Dy and Sm-doped Sr_2SiO_4.

In order to compensate for oscillations in the absorption spectra, $\mu(E)$ has been converted to an absorption function $\chi(E)$ defined as follows:[23]

$$\chi(E) = \frac{\mu(E) - \mu_0(E)}{\Delta\mu_0(E_0)} \quad (2)$$

where E_0 is the absorption edge energy, $\mu_0(E_0)$ is the bare-atom background and $\Delta\mu_0(E_0)$ is the step in the value of $\mu(E)$ at the absorption edge. The energy-dependent absorption coefficient $\chi(E)$ has been converted to a wavenumber-dependent absorption coefficient $\chi(k)$ using the relation:

$$K = \sqrt{\frac{2m(E - E_0)}{\hbar^2}} \quad (3)$$

where m is the mass of an electron and $\hbar$ is Planck's constant. $\chi(k)$ is weighted by k^2 to amplify oscillations at high values of k and the $\chi(k)k^2$ functions are Fourier-transformed in R space to

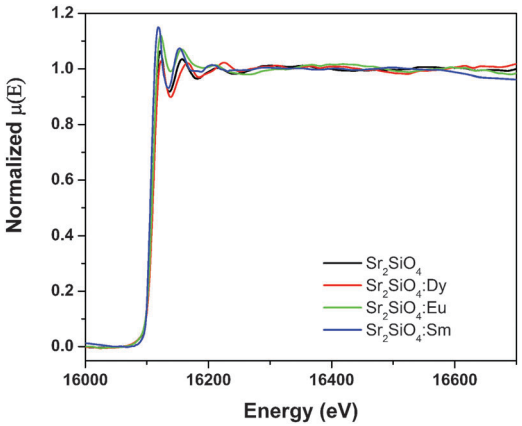

Fig. 11 Normalized EXAFS spectra of blank Sr_2SiO_4 along with Eu, Dy and Sm-doped Sr_2SiO_4.

generate the spectra of $\chi(R)$ *versus* R in terms of real distances from the center of the absorbing atom. The EXAFS data analysis set available within the IFEFFIT software package has been used for EXAFS data analysis.[24] This includes the background reduction and Fourier transform to derive spectra of $\chi(R)$ *versus* R from the absorption spectra (using ATHENA software), generation of theoretical EXAFS spectra starting from an assumed crystallographic structure and finally fitting of experimental data to the theoretical spectra using ARTEMIS software.

The spectra of $\chi(R)$ *versus* R have been generated for all the samples from the spectra of $\mu(E)$ *versus* E following the methodology described above and the best-fit spectra of $\chi(R)$ *versus* R of the samples are shown in Fig. 12. The structural parameters (atomic coordination and lattice parameters) of Sr_2SiO_4 that were used for the simulation of theoretical EXAFS spectra of the samples were obtained from values reported in the literature.[10,13] There are two crystallographic sites of strontium in the structure, of which one is 10-coordinated and the other is 9-coordinated. Scattering paths were generated using each Sr atom as central atom and were used in fitting the experimental data with 50% weightage given to each crystallographic site. The bond distances, coordination numbers (including scattering amplitudes) and disorder (Debye–Waller) factors (σ^2), which give the mean square fluctuations in the distances, were used as fitting parameters and are summarized in tabular form (ESI,† Table T3).

3.3.2. Eu-doped Sr_2SiO_4. From EXAFS data (ESI,† Table T3), it is seen that average bond lengths remain unchanged on doping with Eu, which can be explained by the fact that the ionic radii of 10-coordinated Eu^{2+} (1.35 Å) and 9-coordinated Eu^{2+} (1.30 Å) are close to those of 10-coordinated Sr^{2+} (1.36 Å) and 9-coordinated Sr^{2+} (1.31 Å), respectively.[25] There is an increase in σ^2 values for both Sr(1)–O and Sr(2)–O bonds, which gives evidence of an increase in disorder at both the Sr sites and thus corroborates the earlier results that Eu is incorporated at both 10- and 9-coordinated sites. However, it has been observed that the change in σ^2 value is higher for 9-coordinated Sr sites than for 10-coordinated Sr sites, which may be due to the greater incorporation of Eu at 9-coordinated sites than at 10-coordinated sites. Nguyen *et al.*[26]

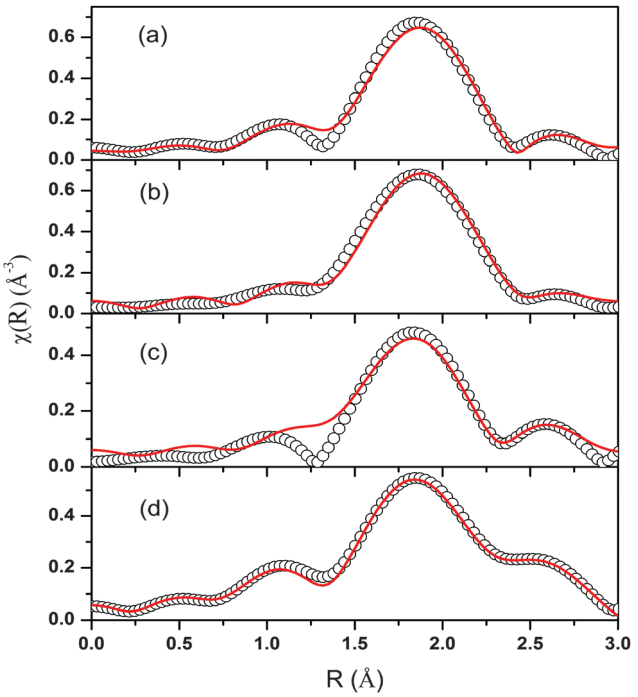

Fig. 12 Fourier-transformed EXAFS spectra at Sr K-edge (scatter points) and theoretical fit (solid line) for (a) Sr_2SiO_4 (b) Dy-doped Sr_2SiO_4 (c) Eu-doped Sr_2SiO_4 and (d) Sm-doped Sr_2SiO_4.

also reported the preferentially higher substitution of Eu at 9-coordinated Sr sites on the basis of enhanced intensity of yellow luminescence.

3.3.3. Dy-doped Sr_2SiO_4. The average Sr(2)–O bond length was found to decrease in Dy-doped samples compared to undoped samples (ESI,† Table T3); however, no change appeared in the average Sr(1)–O bond length. This decrease in Sr(2)–O bond length could be due to the smaller ionic size of Dy^{3+} (1.083 Å for 9-coordination) than Sr^{2+} (1.31 Å for 9-coordination).[25] It may be possible that Dy ions only occupy Sr(2) sites and not Sr(1) sites, as 10-coordinated geometry of Dy does not exist;[25] however, EXAFS measurements at the Dy edge are required to ascertain this.

3.3.4. Sm-doped Sr_2SiO_4. The average Sr(1)–O and Sr(2)–O bond lengths were found to decrease (ESI,† Table T3) in Sm-doped samples compared to undoped samples. It is also observed that σ^2, which is the mean square displacement parameter, increases for Sr(2)–O bonds, which indicates that 9-coordinated Sr sites are replaced by Sm ions.

3.4. Computational results

In order to rationalize the experimental results and to get insight into the local structure, theoretical calculations were carried out on Sr_2SiO_4 (undoped and doped with Eu/Sm/Dy atoms). All calculations were carried out using spin-polarized DFT with a plane-wave basis set implemented in the Vienna Ab-initio Simulation Package (VASP). Electron–ion interactions were described by the projector augmented wave (PAW) method. The spin-polarized generalized gradient approximation using the Perdew–Burke–Ernzerhof (PBE) functional has been used

to calculate the exchange–correlation energy. The cut-off energy for the plane-wave basis set was fixed at 400 eV. Geometry optimization was performed by ionic relaxation using a conjugate gradient minimization. Geometries were considered to be converged when the force on each ion became 0.01 eV $Å^{-1}$ or less. The total energy convergence was tested with respect to the sizes of the plane-wave basis set and the simulation cell and the total energy was found to be accurate to within 1 meV. Three-dimensional periodic boundary conditions were applied to approximate a bulk solid (*i.e.* the orthorhombic phase of Sr_2SiO_4). A conventional cubic unit ($\alpha = \beta = \gamma = 90^\circ$) cell containing 28 atoms (8 Sr, 4 Si, 16 O) was used for calculations. Structural optimization was performed with respect to atomic coordinates and unit cell parameters. A Monkhorst–Pack *k*-point grid of 3 × 3 × 3 was employed to map the first Brillouin zone. For the orthorhombic unit cell, the lattice parameters were found to be a = 5.673 Å, b = 7.073 Å and c = 9.766 Å. These values are excellent in comparison to the experimental lattice constants (a = 5.682 Å, b = 7.091 Å and c = 9.772 Å). In the case of doped Sr_2SiO_4, out of the 8 Sr atoms in the unit cell, one atom was replaced with a Eu/Sm/Dy atom. As mentioned previously, two types of Sr atom (9-coordinated and 10-coordinated) are present in Sr_2SiO_4; therefore, both 9- and 10-coordinated sites were considered for replacement and optimizations were carried out without any symmetry constraints. The energetics of the doped structures are tabulated (ESI,† Table T4).

In terms of energetics, it is clear that the 9-coordinated site is more favourable than its 10-coordinated counterpart (ESI,† Table T4). However, it can be noted that the difference in stability for Eu^{3+} doping between 9- and 10-coordinated sites is only 0.03 eV (of the order of room-temperature energy). In contrast, for Dy and Sm doping, the difference in stability between the two sites is much higher (~0.6–0.7 eV). These results are in excellent agreement with those obtained by experimental methods, where both Dy and Sm were found to occupy only 9-coordinated sites and the presence of Eu at both 9- and 10-coordinated sites was reported. Therefore, it can be inferred that the destabilization of 10-coordinated occupancy by a strong metal–oxygen bond for Dy and Sm is the cause of such an observation.

In order to further rationalize the results, we focused our attention on the geometrical aspects of the SrO_9 and SrO_{10} polyhedra of Sr_2SiO_4. In SrO_9 polyhedra, the average Sr–O bond length was found to be 2.68 Å (shortest bond: 2.50 Å, longest bond: 3.04 Å) and for SrO_{10} polyhedra, the average Sr–O bond length was found to be 2.84 Å (shortest bond: 2.38 Å, longest bond: 3.04 Å) (ESI,† Fig. S5 and S6). The theoretically calculated values of the average Sr–O bond length in SrO_9 and SrO_{10} polyhedra are in agreement with the experimental values of 2.698 Å and 2.852.[13] Further symmetry observations for these two polyhedra (C_{2v} for SrO_9 and C_{3v} for SrO_{10}) are shown in Fig. 13 and tabulated (ESI,† Table T5). It can be seen from the table that SrO_9 has lower symmetry of C_{2v} than that of SrO_{10}, which has C_{3v} symmetry. The relatively higher symmetry of SrO_{10} polyhedra is in line with the experimental result presented in Section 3.2.2, as well as previous reports.[10]

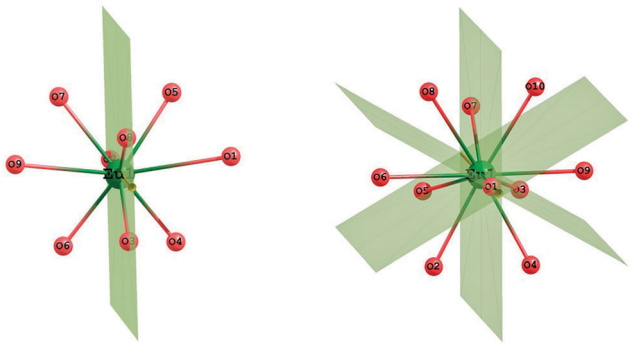

Fig. 13 Nearest high-end symmetry observed for SrO_9 and SrO_{10}.

Importantly, SrO_{10} polyhedra have a short Sr–O bond at 2.38 Å, which is not present in SrO_9 polyhedra. Furthermore, we noticed that the substitution of Eu at Sr does not distort the original SrO_9 and SrO_{10} polyhedra (ESI,† Fig. S7), but the inclusion of Dy and Sm leads to the distortion of polyhedra to a greater extent (ESI,† Fig. S8 and S9). In particular, the substitution of Sr in SrO_{10} polyhedra by Dy and Sm leads to substantial changes by reducing the length of the shortest metal–oxygen bond from 2.38 Å in the original SrO_{10} polyhedra to 2.18/2.29 Å, respectively. Simultaneously, few other M–O bonds were also reduced in length. The contraction of these M–O bonds leads to the elongation of some other M–O bonds (from 2.8–3.0 Å in the original SrO_{10} polyhedra to 2.9–3.5/2.9–3.2 Å for DyO_{10}/SmO_{10}). This observed distortion is in line with the energetics values presented in Table T4 (ESI†), where the difference in stability for substitution by Dy and Sm at 9- and 10-coordinated sites was found to be quite large at ~0.6–0.7 eV. It can be noted that despite the ionic radii of these three cations, Sm^{3+} (1.13 Å), Eu^{3+} (1.12 Å), and Dy^{3+} (1.09 Å) being comparable with that of the Sr^{2+} ion, the strength of the metal–oxygen bond in the M–O dimer (M = Eu, Dy, Sm) is quite different for the three. The values in eV per atom follow the following trend: Sr–O (2.66) < Eu–O (2.95) < Sm–O (3.58) < Dy–O (3.84).[27]

Therefore, on the basis of these results, it is inferred that Dy and Sm form much stronger bonds with oxygen in comparison to Sr and Eu (Sr and Eu have comparable values). The stability of Dy–O/Sm–O bonds leads to the formation of a few strong metal–oxygen bonds in DyO_{10}/SmO_{10} by losing other metal–oxygen bonds in the polyhedra. Thus, the relatively enhanced stability of Dy–O/Sm–O bonds leads to the contraction of a few metal–oxygen bonds. As a consequence, the remaining metal–oxygen bonds become weaker or elongated. This asymmetrical contraction/elongation phenomenon in the DyO_{10}/SmO_{10} polyhedron leads to significant distortion with respect to the original SrO_{10} polyhedra. These results explain very well that in experiments, a Eu atom could substitute Sr at both 9- and 10-coordinated sites; however, Dy and Sm could not substitute Sr at 10-coordinated sites.

3.5. Conclusions

In the present study, we carried out an exhaustive experimental and theoretical investigation to get in-depth knowledge of the local symmetry of SrO_9 and SrO_{10} polyhedra in Sr_2SiO_4.

Undoped and lanthanide ion-doped (Eu, Dy and Sm) Sr_2SiO_4 have been synthesized using a sol–gel method and characterized using XRD and photoluminescence (PL) spectroscopy. In terms of structure, it was found that there are two types of strontium polyhedra in strontium silicate: asymmetric SrO_9 and relatively symmetric SrO_{10}. The local point groups of these two polyhedra were determined using emission spectroscopy taking europium as the probe ion, which was further supported by theoretical measurements. Based on PL data and emission dynamics, it was inferred that Eu occupies both 9- and 10-coordinated Sr sites in strontium silicate, whereas Sm and Dy occupy specifically 9-coordinated Sr sites only. These results were further corroborated using Sr K-edge extended X-ray absorption fine structure (EXAFS) measurements. Theoretical calculations using DFT also suggested that energetically Eu is stable in both SrO_9 and SrO_{10} polyhedra, whereas Sm and Dy destabilize 10-coordinated Sr polyhedra by strengthening individual metal–oxygen bonds.

References

1 J. Y. Park, M. A. Lim, C. H. Kim, H. D. Park, J. T. Park and S. Y. Choi, *Appl. Phys. Lett.*, 2003, **82**, 683–685.
2 N. Lakshminarasimhan and U. V. Varadaraju, *J. Electrochem. Soc.*, 2005, **152**, H152–H156.
3 D. V. Sunitha, H. Nagabhushana, S. C. Sharma, B. M. Nagabhushana, B. Daruka Prasad and R. P. S. Chakradhar, *Spectrochim. Acta, Part A*, 2014, **127**, 381–387.
4 H. Nagabhushana, D. V. Sunitha, S. C. Sharma, B. Daruka Prasad, B. M. Nagabhushana and R. P. S. Chakradhar, *J. Alloys Compd.*, 2014, **595**, 192–199.
5 Z. Song, X. Ding, S. Yang, F. Du, L. Bian, S. Duan and Q. L. Liu, *J. Lumin.*, 2014, **152**, 199–202.
6 J. Barzowska, A. Chruścińska, K. Przegietka and K. Szczodrowski, *Radiat. Phys. Chem.*, 2014, **104**, 31–35.
7 M. A. Tshabalala, H. C. Swart and O. M. Ntwaeaborwa, *J. Vac. Sci. Technol., A*, 2014, **32**, 021401.
8 X. Xu, X. Zhang, T. Wang, J. Qiu and X. Yu, *Mater. Lett.*, 2014, **127**, 40–43.
9 J. Qin, B. Lei, J. Li, Y. Liu, H. Zhang, M. Zheng, Y. Xiao and K. Chao, *ECS J. Solid State Sci. Technol.*, 2013, **2**, R60–R64.
10 M. Catti, G. Gazzoni and G. Ivaldi, *Acta Crystallogr., Sect. C*, 1983, **39**, 29–34.
11 S. K. Gupta, N. Pathak, S. K. Thulasidas and V. Natarajan, *J. Lumin.*, 2014, DOI: 10.1016/j.jlumin.2014.10.009.
12 S. K. Gupta, M. K. Bhide, R. M. Kadam, V. Natarajan and S. V. Godbole, *J. Exp. Nanosci.*, 2015, **10**, 610–621.
13 S. K. Gupta, M. Mohapatra, S. Kaity, V. Natarajan and S. V. Godbole, *J. Lumin.*, 2012, **132**, 1329–1338.
14 S. K. Gupta, M. Kumar, V. Natarajan and S. V. Godbole, *Opt. Mater.*, 2013, **35**, 2320–2328.
15 S. Basu, D. K. Patel, J. Nuwad, S. N. Jha, D. Bhattacharyya, V. Sudarsan, R. K. Vatsa and S. K. Kulshreshtha, *Chem. Phys. Lett.*, 2013, **561–562**, 82–86.
16 S. Basu, S. Varma, A. N. Shirsat, B. N. Wani, S. R. Bharadwaj, A. Chakrabarti, S. N. Jha and D. Bhattacharyya, *J. Appl. Phys.*, 2012, **113**, 043508.
17 N. L. Misra, A. K. Yadav, S. Dhara, R. Phatak, S. K. Mishra, A. K. Poswal, S. N. Jha, A. K. Sinha and D. Bhattacharyya, *Anal. Sci.*, 2013, **29**, 579.
18 J. Yang, L. Yang, W. Liu, Y. Zhang, H. Fan, Y. Wang, H. Liu, J. Lang and D. Wang, *J. Alloys Compd.*, 2008, **454**, 506.
19 A. Nag and T. R. N. Kutty, *J. Mater. Chem.*, 2004, **14**, 1598–1604.
20 X. Y. Chen and G. K. Liu, *J. Solid State Chem.*, 2005, **178**, 419–428.
21 X. Y. Chen, W. Zhao, R. E. Cook and G. K. Liu, *Phys. Rev. B: Condens. Matter Mater. Phys.*, 2004, **70**, 205122.
22 J. Qiang, L. Yongsheng, L. Renfu, L. Liu, L. Wenqin and C. Xueyuan, *J. Phys. Chem. C*, 2009, **113**, 2309–2315.
23 D. C. Konigsberger and R. Prince, in *X-ray Absorption: Principles, Applications, Techniques of EXAFS, SEXAFS and XANES*, ed. D. C. Konigsberger and R. Prins, Wiley & Sons, New York, 1988.
24 M. Newville, B. Ravel, D. Haskel, J. J. Rehr, E. A. Stern and Y. Yacoby, *Physica B*, 1995, **208**, 154–156.
25 R. D. Shannon, *Acta Crystallogr., Sect. A: Cryst. Phys., Diffr., Theor. Gen. Crystallogr.*, 1976, **32**, 751–767.
26 H.-D. Nguyen, I.-H. Yeo and S.-I. Mho, *ECS Trans.*, 2010, **28**, 167–173.
27 W. M. Haynes, *CRC Handbook of Physics and Chemistry*, 94th edn, 2013.